Phase Engineering of Molybdenum Carbide via Vanadium Doping for Boosted Hydrogen Evolution Reaction in Water Electrolysis

Songjie Li , Yuxin Li , Renzhe Jin , Jiajiao Wei , Peng Zhu , Jianmeng Wu , Xiaomei Yu * , Jinyou Zheng *

Posted Date: 14 January 2026

doi: 10.20944/preprints202601.0934.v1

Keywords: molybdenum carbide; phase engineering; hydrogen evolution reaction; heteroatom

 doi:10.20944/preprints202601.0934.v1

Article

Phase Engineering of Molybdenum Carbide via Vanadium Doping for Boosted Hydrogen Evolution Reaction in Water Electrolysis

Songjie Li [1,2], Yuxin Li [1], Renzhe Jin [1], Jiajiao Wei [1], Peng Zhu [1], Jianmeng Wu [1], Xiaomei Yu [1,2,*] and Jinyou Zheng [1,2,*]

[1] School of Chemical Engineering, Zhengzhou University, 100 Science Avenue, Zhengzhou 450001, China
[2] Engineering Research Center of Advanced Functional Material Manufacturing of Ministry of Education, Zhengzhou University, 100 Science Avenue, Zhengzhou 450001, China
* Correspondence: jinyouzh@zzu.edu.cn (J.Z.); yuxm@zzu.edu.cn (X.Y.)

Abstract

Efficient and low-cost electrocatalysts play a crucial role in hydrogen production through electrolysis of water. Molybdenum (Mo) carbide with a similar electronic structure to Pt was selected, both α-MoC_{1-x} and α-MoC_{1-x}/β-Mo_2C electrocatalysts were successfully fabricated for electrochemical hydrogen evolution. A continuous optimization of the hydrothermal and carbonization conditions was carried out for the preparation of α-MoC_{1-x}. The biphasic molybdenum carbide catalysts were further achieved via vanadium doping with a phase transition of molybdenum carbide from α to β, which increases the specific surface area of the electrocatalyst. It was found that the V-Mo_xC catalyst obtained at a Mo/V molar ratio of 100:5 exhibited the best hydrogen production performance, with a β to α phase ratio of 0.827. The overpotential of V-Mo_xC at η_{10} decreased to 99 mV, and the Tafel slope reached 65.1 mV dec^{-1}, indicating a significant improvement in performance compared to undoped samples. Excellent stability was obtained of the as-prepared electrocatalyst for water splitting over 100 h at a current density of 10 mA cm^{-2}.

Keywords: molybdenum carbide; phase engineering; hydrogen evolution reaction; heteroatom

1. Introduction

With the rapid advancement of society, the global demand for energy has surged. Currently, non-renewable energy sources such as oil, coal, and natural gas still dominate the energy landscape. However, their excessive use has led to growing concerns over energy shortages and environmental pollution [1–3], resulting in an urgent need to develop clean and sustainable alternatives [4]. Hydrogen energy has attracted increasing attention due to its zero emissions, recyclability, and high energy density [5]. The water electrolysis is considered one of the most promising methods for green hydrogen generation due to its environmental friendliness and renewability. Water electrolysis involves two half-reactions: oxygen evolution reaction (OER) at the anode and hydrogen evolution reaction (HER) at the cathode [6,7]. Platinum exhibits the highest catalytic performance for HER among noble metals, with low Tafel slopes and minimal overpotentials [8]. However, its high cost, scarcity, and poor stability under harsh conditions limit large-scale applications. Molybdenum (Mo), as one of the abundant transition metals on Earth, has been widely applied due to its excellent physicochemical properties [9]. Mo-based materials have been extensively studied in the field of energy conversion, including molybdenum oxides, molybdenum disulfide, and molybdenum carbides [10–12]. Among them, molybdenum carbide is considered an effective non-noble metal catalyst due to its Pt-like d-band electron density, high electrical conductivity and stability. Kitchin et al. found that when molybdenum combines with carbon to form molybdenum carbide, the surface

 doi:10.20944/preprints202601.0934.v1

d-band becomes broader than that of Mo, showing new bonding characteristics [13]. Li et al. developed novel Mo_2C NTs via an organic-inorganic hybrid approach, and discovered their exceptional electrocatalytic performance for hydrogen evolution under alkaline conditions [14]. Yu et al. prepared N-Mo_xC/CoP-0.5 by decorating CoP with N-Mo_xC, which exhibits excellent electrocatalytic activity for the hydrogen evolution reaction (HER). The N-Mo_xC modification preserves CoP's fast charge transfer kinetics while expanding the active surface area, providing abundant interfaces and active sites for HER [15].To date, various crystal phases of molybdenum carbide have been extensively investigated, including face-centered cubic α-MoC_{1-x}, simple hexagonal γ-MoC, and hexagonal close-packed β-Mo_2C. Differences in atomic stacking and surface energy among these phases result in distinct electrochemical properties [16,17].

Initially regarded as a support material for Pt, molybdenum carbide was later found to possess intrinsic HER activity [18]. In 2012, Hu et al. demonstrated that commercial β-Mo_2C exhibits excellent HER performance in both acidic and alkaline media [19]. Density functional theory (DFT) calculations revealed that the overlap between Mo d-orbitals and C p-orbitals leads to a broadened d-band, contributing to its Pt-like electronic structure and high catalytic activity [13]. Wan et al. synthesized four different phases of molybdenum carbide and investigated their crystal structures and HER performance [20]. They found a strong correlation between the HER activity and the surface electronic configurations of the different phases. The HER performance followed the order: α-MoC_{1-x} < η-MoC < γ-MoC < β-Mo_2C. Numerous theoretical and experimental studies have also confirmed that the HER activity of molybdenum carbide, similar to that of tungsten carbides, is strongly dependent on its crystal phase [21]. Although Mo-based carbides have been extensively studied as HER catalysts, their activity and stability still fall short of industrial standards.

To achieve this, researchers have employed strategies such as heteroatom doping, phase engineering, and heterostructure construction to enhance intrinsic activity. Yu et al. investigated the activity of Mo_2C doped with various transition metals [22]. Both DFT calculations and electrochemical experiments demonstrated that the introduction of transition metals significantly alters the hydrogen adsorption energy and catalytic activity of Mo_2C. The synergistic effects between different phases result in much higher catalytic performance for multiphase catalysts compared to their single-phase counterparts [23]. Chen et al. successfully induced a phase transition from β-Mo_2C to α-MoC_{1-x} through boron doping, with the amount of α-MoC_{1-x} increasing as the B content rose [24]. The formation of a β-Mo_2C/α-MoC_{1-x} heterostructure led to the exposure of more active sites, enhancing the catalytic performance.

Inspired by these findings, this work first investigated the optimal preparation conditions for α-MoC_{1-x} and subsequently employed ammonium metavanadate as the vanadium source. By precisely tuning the vanadium content, a series of V-Mo_xC samples with varying compositions were obtained. We systematically examined the effects of vanadium doping on crystal structure, morphology, electronic properties, and HER performance. The results demonstrate that vanadium can effectively induce the transformation of α-MoC_{1-x} into biphasic α-MoC_{1-x}/β-Mo_2C materials. This study provides an effective strategy for designing high-performance HER catalysts through controlled phase engineering.

2. Results and Discussion

 doi:10.20944/preprints202601.0934.v1

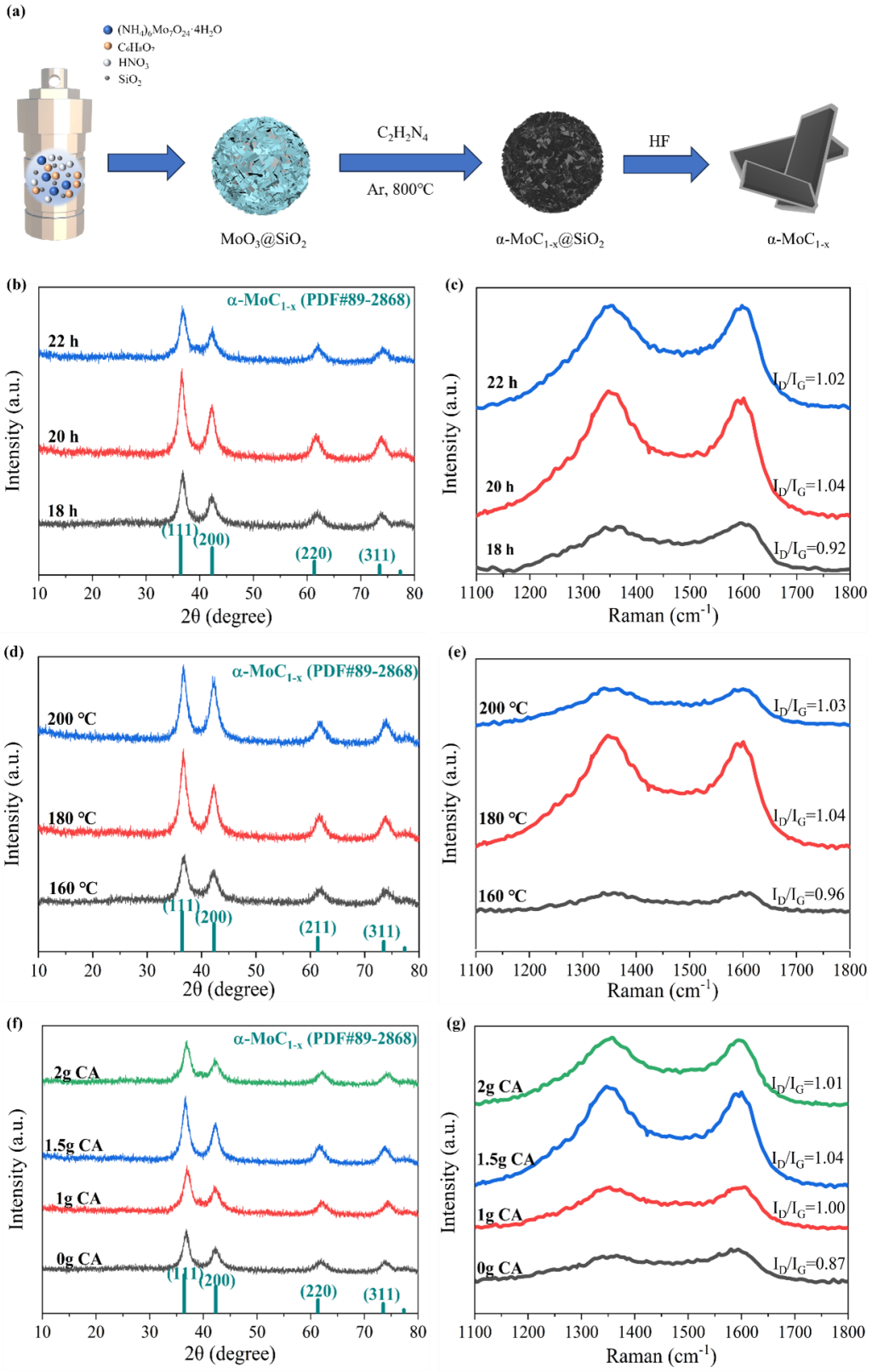

Figure 1. (a) Preparation processes of α-MoC_{1-x}. (b, d, f) XRD patterns and (c, e, g) Raman spectra of α-MoC_{1-x} samples prepared under different hydrothermal conditions.

A study on the structure of the as prepared α-MoC_{1-x} electrocatalyst under different hydrothermal conditions was conducted using XRD and Raman spectroscopy, as shown in Figure 1(b-g). The XRD patterns of the as-prepared electrocatalyst in Figure 1(b, d, f) exhibit a cubic α-MoC_{1-x} crystal phase [25], the specific diffraction peaks at 2θ of 36.5°, 42.3°, 61.7°, and 73.8°, which assigned to the (111), (200), (220), and (311) crystal planes of α-MoC_{1-x}, respectively. The full width at half

 doi:10.20944/preprints202601.0934.v1

maximum (FWHM) of the diffraction peaks for α-MoC_{1-x} prepared under different conditions varies slightly, indicating that the crystallite sizes are approximately similar. It was found that the highest crystallinity of α-MoC_{1-x} was achieved under hydrothermal conditions using 1.5 g of citric acid at 180 °C for 20 h. The molecular structure of the as-prepared α-MoC_{1-x} electrocatalysts obtained under different hydrothermal conditions were investigated by Raman spectra, shown in Figure 1(c, e, g). The peaks at approximately 1349 cm^{-1} and 1593 cm^{-1} correspond to the D and G bands of carbon materials, respectively [26]. The intensity of the D bands is related to the defect density in the material, while the G bands represents the graphitic structure, corresponding to the vibration of sp^2-hybridized carbon atoms, reflecting the degree of graphitization and lattice integrity. A higher ID/IG ratio typically indicates a greater concentration of structural defects and lower graphitization, whereas a lower ratio suggests fewer defects and higher graphitization. Comparative analysis revealed that the sample prepared with 1.5 g of citric acid under hydrothermal conditions at 180 °C for 20 h exhibited both favorable stability and catalytic activity. Therefore, these parameters were established as the optimal conditions for synthesizing the α-MoC_{1-x} precursor.

Moreover, the effect of the amount of carbon source (dicyandiamide, DCD) and the carbonization temperature during the carburization process was investigated. The phase composition and structural properties of the resulting products under different carbonization conditions were studied using XRD and Raman spectroscopy, shown in Figure 2. When the mass ratios of precursor to DCD were set at 1:1, 1:2, 1:3, and 1:4, the XRD patterns of all products exhibited diffraction peaks exclusively corresponding to α-MoC_{1-x}, with no additional impurity phases detected. However, the amount of DCD significantly influenced the crystallinity and crystallite size of the material, as evidenced by variations in peak intensity and full width at half maximum (FWHM) in the XRD patterns. As the DCD content increased, the peak intensity initially increased and then gradually decreased, reaching its maximum at a precursor-to-DCD ratio of 1:2. Meanwhile, the FWHM progressively broadened with higher DCD loading, indicating a reduction in crystallite size (Figure 2a).

In contrast, the carbonization temperature had a more pronounced impact on the material's phase composition and structure. As shown in Figure 2c, the samples carbonized at 600 °C, 700 °C, and 800 °C all retained the characteristic peaks of α-MoC_{1-x}. However, when the temperature reached 900 °C, partial decomposition occurred, leading to the formation of β-Mo_2C. At 600 °C, the material exhibited poor crystallinity, likely due to insufficient carbonization. The Raman spectra (Figure 2(b-d)) further revealed structural changes under different carbonization conditions. The results indicate that the sample prepared with a precursor-to-dicyandiamide mass ratio of 1:2 and carbonized at 800 °C exhibited the highest ID/IG ratio, suggesting an optimal balance between defect density and graphitic ordering. The slight decrease in the ID/IG ratio at higher temperatures may be attributed to excessive thermal energy promoting carbon atom rearrangement, thereby reducing structural disorder. Therefore, these conditions (1:2 mass ratio, 800 °C) were selected as the optimal carbonization parameters for subsequent material synthesis, ensuring a favorable defect-rich carbon structure while maintaining phase purity and crystallinity.

 doi:10.20944/preprints202601.0934.v1

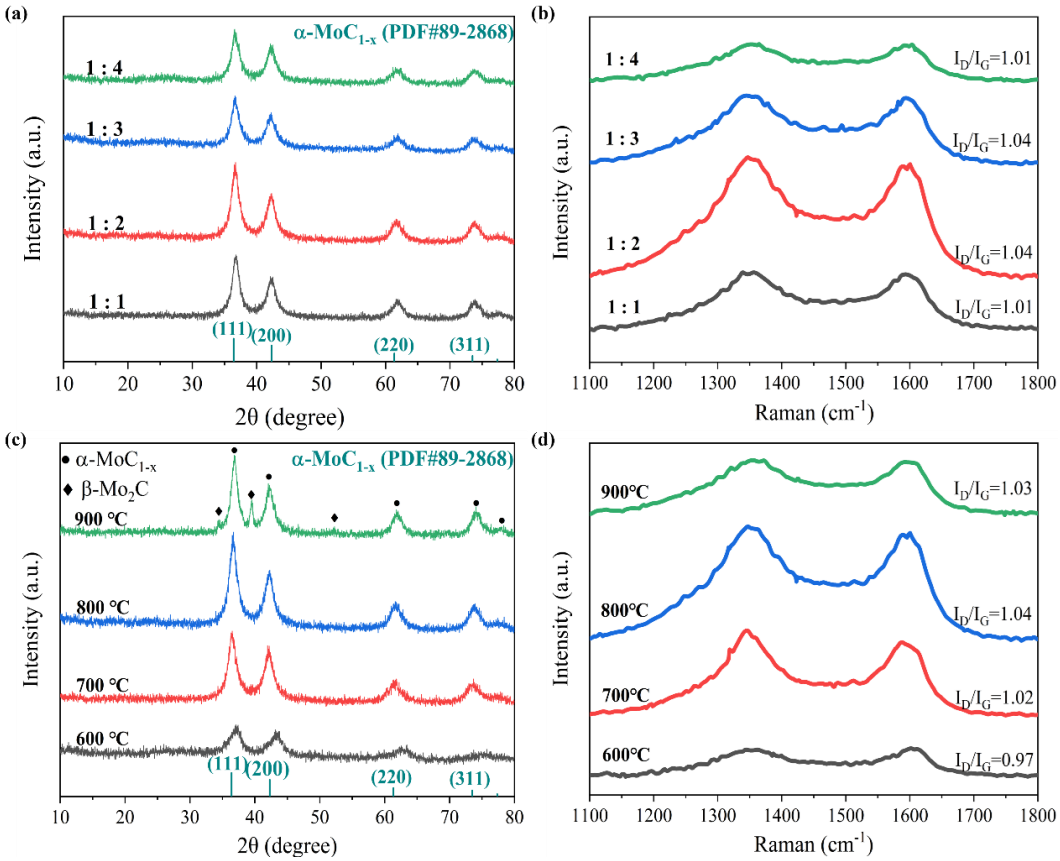

Figure 2. (a, c) XRD and (b, d) Raman spectra of α-MoC_{1-x} samples prepared under different carbonation conditions.

The V-doping was illustrated in Figure 3a for the preparation of V-Mo_xC. From Figure 3b the XRD patterns of V-Mo_xC samples prepared under identical conditions with varying vanadium content. No distinct V-related peaks are observed in any sample, indicating high dispersion of vanadium within the material [27]. At a Mo/V molar ratio of 100:2, only characteristic peaks of α-MoC_{1-x} appear at 36.4°, 42.0°, 61.7°, and 73.7°, corresponding to the (111), (200), (220), and (311) planes, respectively, suggesting that the α-to-β phase transition has not occurred due to insufficient V content. As the V content increases to a Mo/V ratio of 100:5, the transition from α-MoC_{1-x} to β-Mo_2C is initiated, evidenced by the emergence of (100) and (101) peaks at 34.4° and 39.3°, respectively. These β-Mo_2C peaks intensify with further V addition, and at a ratio of 100:11, additional peaks at 52.0° and 69.5° corresponding to the (102) and (103) planes appear, indicating enhanced phase transformation from α-MoC_{1-x} to β-Mo_2C. In Figure 3c, the Raman spectra show that the sample with the lowest V content (Mo/V = 100:2) has the lowest ID/IG ratio (0.96), while others range from 1.01 to 1.07, indicating more disordered carbon. The low ID/IG value at low V content suggests a single-phase α-MoC_{1-x} structure with a relatively smooth and graphitized carbon surface. In contrast, the formation of α-MoC_{1-x}/β-Mo_2C biphasic structure at higher V content provides rougher surfaces, promoting defect-rich carbon layers and higher ID/IG ratios.

 doi:10.20944/preprints202601.0934.v1

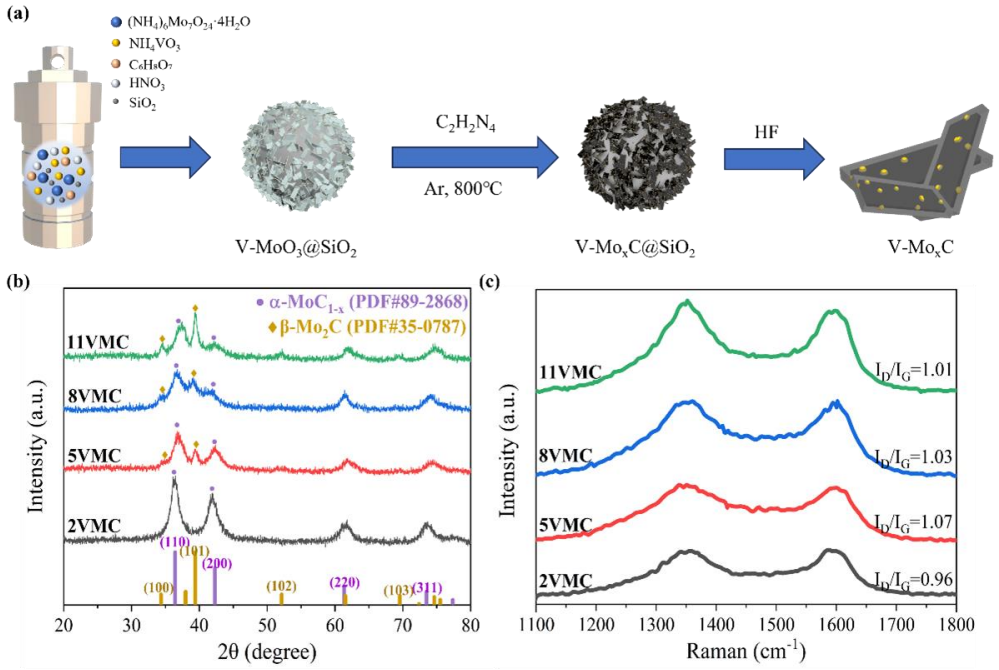

Figure 3. (a) Preparation process of V-MoxC. (b) XRD patterns and (c) Raman spectra of V-MoxC samples prepared with different vanadium doping levels.

Figure 4(a-b) compares the specific surface area and pore size distribution of V-MoxC (Mo/V = 100:5) with pure α-MoC_{1-x}. It should be noted that the α-MoC_{1-x} material discussed here was synthesized under the previously determined optimal conditions. Between the remaining two samples, the V-doped 5VMC exhibits a substantial increase in specific surface area (94.18 $m^2\ g^{-1}$) compared to pure α-MoC_{1-x} (64.67 $m^2\ g^{-1}$), due to the formation of a biphasic structure induced by vanadium doping, which enhances porosity and surface area. The pore size distribution (Figure 4b) reveals that all three materials exhibit mesoporous characteristics, with average pore diameters of 5.30 nm for α-MoC_{1-x}, and 4.68 nm for 5VMC, indicating similar pore structures despite differences in specific surface area.

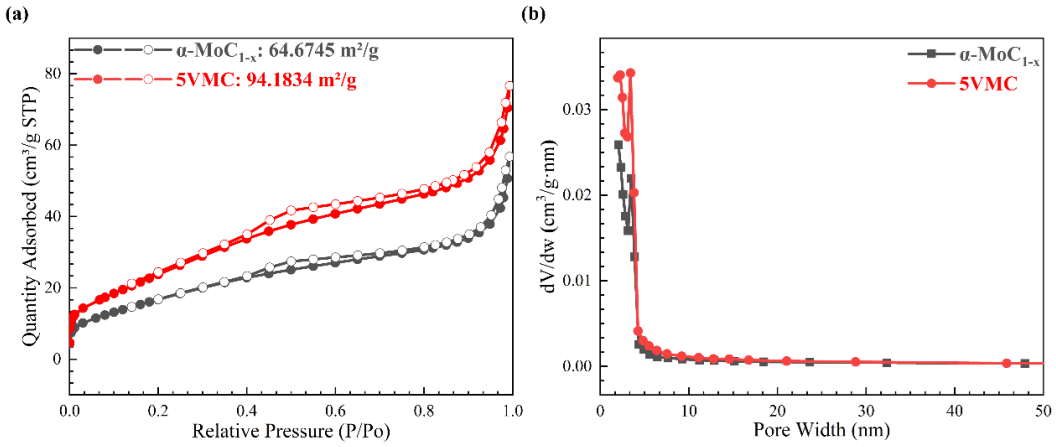

Figure 4. (a) N_2 adsorption-desorption isothermal curves and (b) pore size distributions for α-MoC_{1-x} and 5VMC samples.

 doi:10.20944/preprints202601.0934.v1

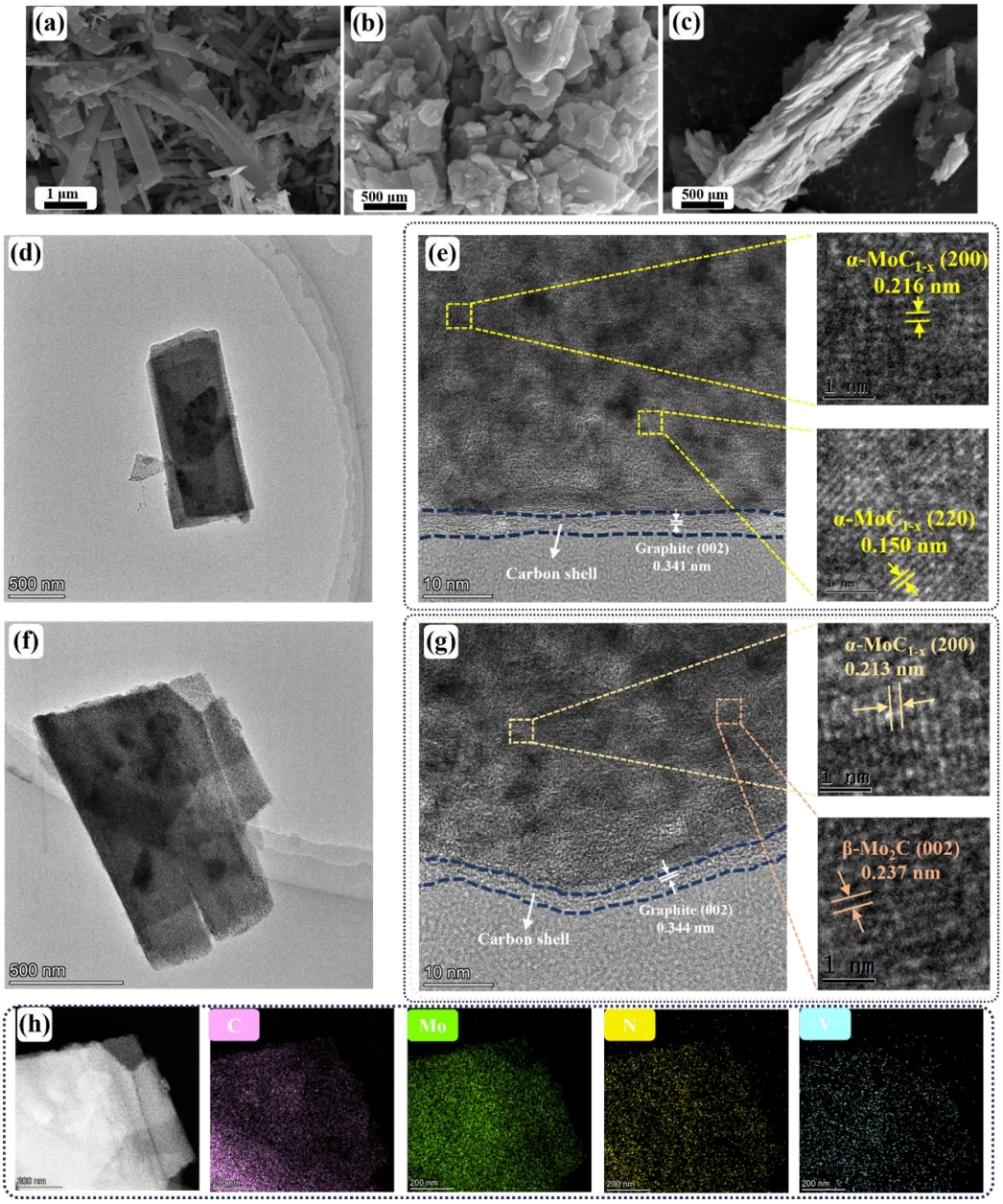

Figure 5. (a) SEM, (d) TEM and (e) HRTEM images of α-MoC_{1-x} prepared under optimal conditions. (b, c) SEM, (f) TEM and (g) HRTEM, and (h) EDS mapping images of 5VMC sample.

The morphologyies of the materials were characterized using SEM and TEM, as illustrated in Figure 5(a-g). From the SEM (Figure 5a) and TEM (Figure 5d) images, it can be observed that the α-MoC_{1-x} retains the plate-like structure of its precursor with relatively uniform dimensions. This two-dimensional morphology facilitates the exposure of active sites, ensuring sufficient contact between the catalyst and electrolyte while enabling rapid release of hydrogen gas during the reaction. The HRTEM (Figure 5e) reveals distinct lattice fringes with spacings of 0.216 nm and 0.15 nm, corresponding to the (200) and (220) crystal planes of α-MoC_{1-x}, respectively. Additionally, the plate-like α-MoC_{1-x} particles are coated with a thin carbon layer (about 4 nm), evidenced by the observed lattice spacing of 0.341 nm, which matches the (002) plane of graphitic carbon. This carbon layer may enhance the material's electronic conductivity and structural stability. Comprehensive characterization of the 5VMC sample by SEM and TEM is presented in Figure 5(b, c, f, g). The material retains the broken, thin, plate-like morphology of the precursor, as shown in Figure 5(b-c). The results of further analysis of the morphology of the material using TEM and HRTEM are shown in Figure 5(f-g). The lattice spacing of 2.13 nm and 2.37 nm in the HRTEM of Figure 5g belongs to the (200)

 doi:10.20944/preprints202601.0934.v1

crystal plane of α-MoC_{1-x} and the (002) crystal plane of β-Mo_2C, respectively, proving the existence of the two phases. The heterostructure formed between them can modulate the local electronic structure and Mo-H bond strength, enhancing HER kinetics [28]. About 3 nm carbon layer is also observed, which stabilizes the structure without hindering electron transfer. As clearly shown in Figure 5h, the material is composed of C, Mo, N, and V elements, confirming the successful doping of V.

The bonding states and quantitative chemical composition before and after vanadium doping were investigated using X-ray photoelectron spectroscopy (XPS), as shown in Figure 6. The Figure 6(a, d) displays the high-resolution XPS spectra of C 1s. The dominant peak at approximately 284.80 eV is attributed to the C-C bond, while the peaks at 283.63 eV, 286.31 eV, and 288.52 eV correspond to C-Mo, C-O/C-N, and C-C=O bonds, respectively [29]. The presence of the C-Mo bond confirms the successful synthesis of molybdenum carbide. The C-N bond indicates the effective doping of nitrogen atoms from the precursor dicyandiamide into the carbon layers, which enhances the catalyst's conductivity [30]. Additionally, nitrogen incorporation induces electron reorganization, activating adjacent carbon atoms and thereby promoting the hydrogen evolution reaction [31]. Figure 6b presents the high-resolution XPS spectrum of Mo 3d, where three pairs of peaks are assigned to Mo-C (228.67/231.82 eV), Mo-N (229.39/232.54 eV) formed between molybdenum and doped nitrogen, and Mo-O (232.80/235.95 eV) due to inevitable molybdenum oxidation [32]. In contrast, Figure 6e shows the high-resolution XPS spectrum of Mo 3d, where two pairs of diffraction peaks at 228.57 eV/231.72 eV and 229.03 eV/232.12 eV correspond to the $3d_{5/2}$ and $3d_{3/2}$ orbitals of Mo^{2+} and Mo^{3+}, respectively. Mo^{2+} is present in β-Mo_2C, while Mo^{3+} exists in α-MoC_{1-x} [33], confirming the coexistence of dual phases. The high-resolution XPS spectrum of N 1s in Figure 6(c, f) can be deconvoluted into five peaks [34]. The diffraction peaks located near 394.98 eV, 397.33 eV, 398.06 eV, 399.45 eV, and 401.82 eV correspond to Mo 3p, Mo-N bond, pyridinic N, pyrrolic N, and graphitic N, respectively. The presence of the Mo-N bond indicates the bonding between N and Mo, which can prevent the dissolution of Mo in the electrolyte, thereby endowing the material with excellent cycling stability. In the high-resolution N 1s spectrum (Figure 6f), the deconvoluted peaks observed at 394.98 eV, 397.33 eV, 398.06 eV, 399.45 eV, and 401.82 eV are assigned to Mo 3p, Mo-N bond, pyridinic N, pyrrolic N, and graphitic N, respectively. The presence of the Mo-N bond confirms the chemical interaction between nitrogen and molybdenum, which effectively suppresses the dissolution of Mo species in the electrolyte and consequently enhances the structural stability of the material. Figure 6g displays the high-resolution XPS spectrum of V 2p, revealing two characteristic doublets corresponding to V^{3+} (514.29 eV/521.79 eV) and V^{4+} (516.17 eV/523.87 eV).

 doi:10.20944/preprints202601.0934.v1

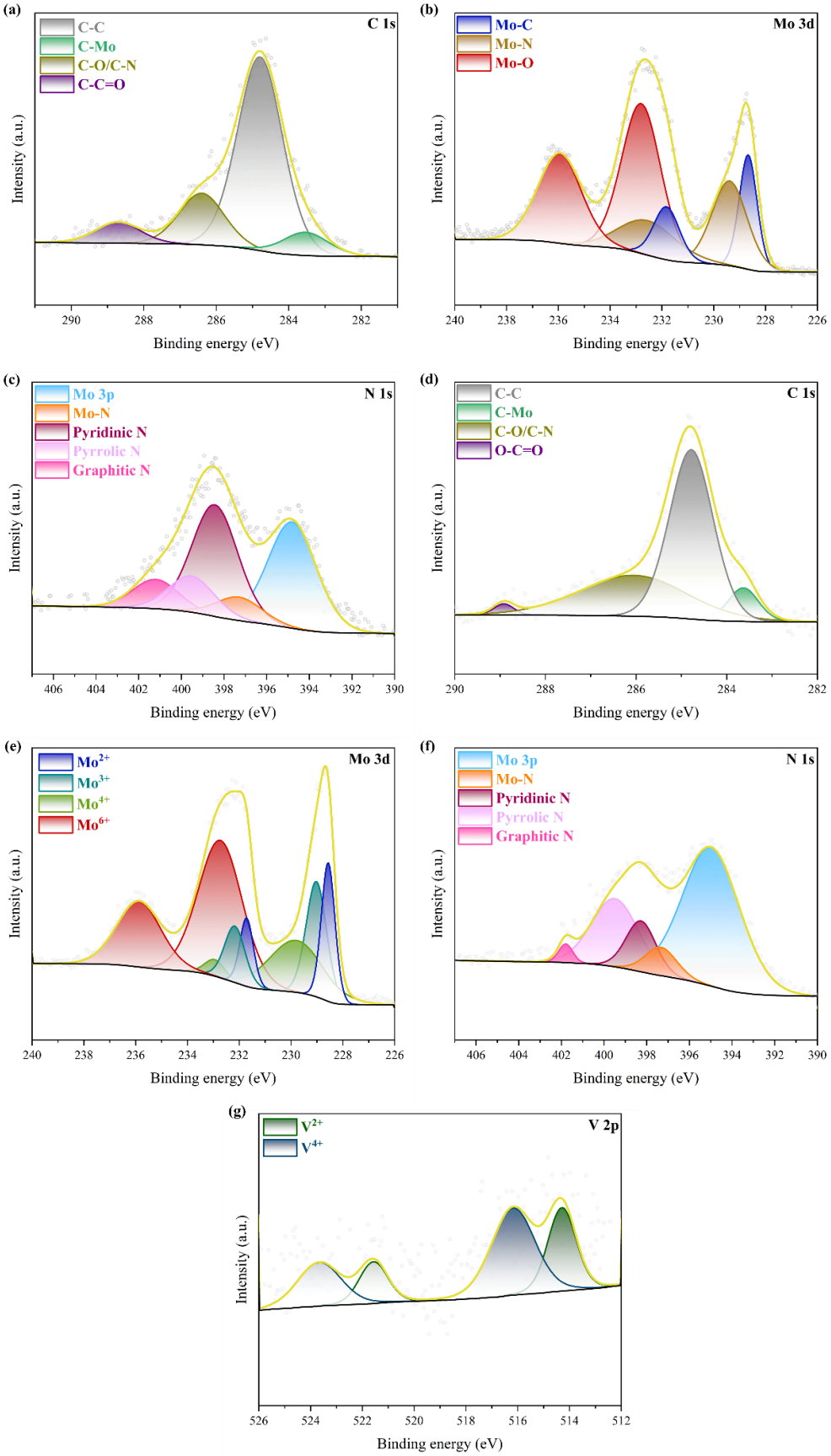

Figure 6. High-resolution XPS spectra of (a) C 1s, (b) Mo 3d and (c) N 1s of α-MoC_{1-x} prepared under the optimum conditions. High-resolution XPS spectra of (d) C 1s, (e) Mo 3d, (f) N 1s and (g) V 2p for 5VMC sample.

 doi:10.20944/preprints202601.0934.v1

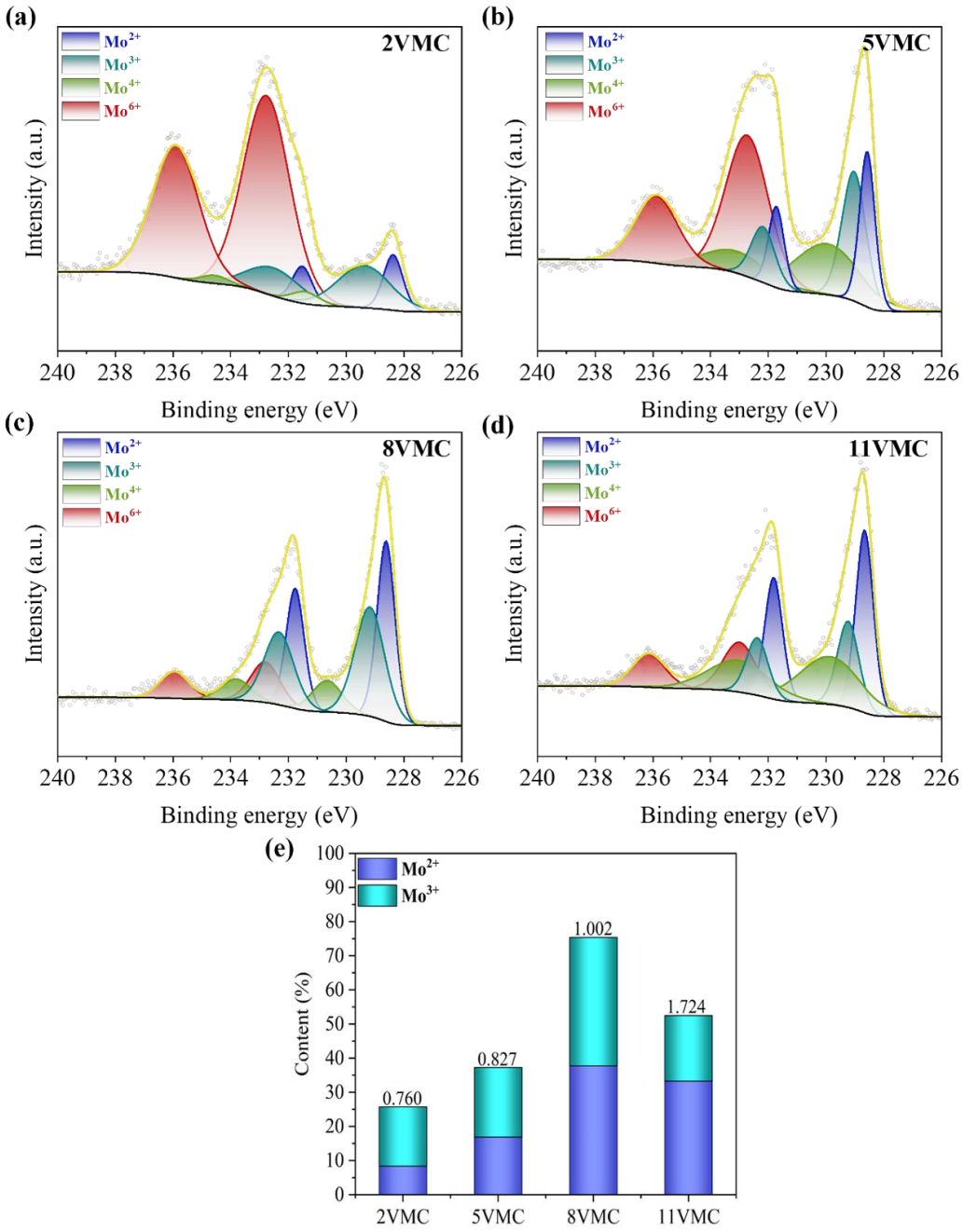

Figure 7. (a-d) Mo 3d high-resolution XPS spectra of samples obtained with different vanadium doping levels and (e) percentage of Mo^{2+} and Mo^{3+} on the surface.

Detailed XPS analysis was conducted on the Mo element in four samples, 2VMC, 5VMC, 8VMC, and 11VMC, as shown in Figure 7(a-d). Previous studies have shown that Mo^{4+} and Mo^{6+} do not contribute significantly to HER activity [35]. Therefore, the study mainly focused on the two valence states of Mo^{2+} and Mo^{3+}. Figure 7e shows the percentage of these two valence states and the Mo^{2+}/Mo^{3+} ratio in the four samples. As mentioned above, Mo^{2+} is contributed by β-Mo_2C, while Mo^{3+} is contributed by α- MoC_{1-x}. Therefore, the change in the ratio of Mo^{2+}/Mo^{3+} can reflect the change in the proportion of β-Mo_2C and α-MoC_{1-x} phases in the material. It is not difficult to see from Figure 7e that with the continuous increase of vanadium element, the Mo^{2+}/Mo^{3+} ratio gradually increases, indicating that the amount of molybdenum carbide in the β phase continues to increase, which is consistent with the XRD results. Further evidence shows that vanadium can induce the transformation of molybdenum carbide from α phase to β phase, and the ratio of the two phases can be controlled by the amount of vanadium added.

 doi:10.20944/preprints202601.0934.v1

Figure 8(a-i) shows the polarization curves, the Tafel slopes, and performance comparison of materials prepared under different hydrothermal conditions. As seen in Figure. 8(a, d, g), the overpotential at 10 mAcm^{-2} (η_{10}) first decreases and then increases with prolonged hydrothermal time and elevated hydrothermal temperature. This trend is attributed to the poor crystallinity of the materials under shorter hydrothermal times and lower hydrothermal temperatures, which negatively affects their reactivity. As the hydrothermal time and temperature increase, the crystallinity of the resulting carbonized products improves, thereby enhancing the catalytic performance. However, when the hydrothermal time and temperature become excessively high, the defect density in the material decreases, leading to a reduction in the exposed active surface area and ultimately resulting in a decline in material performance. The effect of citric acid addition on the material performance exhibits a similar trend to that of hydrothermal temperature and time. To better understand the HER activity from a kinetic perspective, the Tafel slopes of the materials in Figure 8(b, e, h) were obtained from the corresponding polarization curves using the Tafel equation. Generally, a smaller Tafel slope indicates a lower overpotential as the current density increases, suggesting that the catalyst is more efficient in the HER process [36]. As shown in Figure 8(b, e, h), the sample prepared with 1.5 g citric acid addition, 20 h hydrothermal time, and 180 °C hydrothermal temperature exhibits the smallest Tafel slope of 76.3 mV dec^{-1}, indicating fast HER kinetics governed by the Volmer-Heyrovsky process [37].

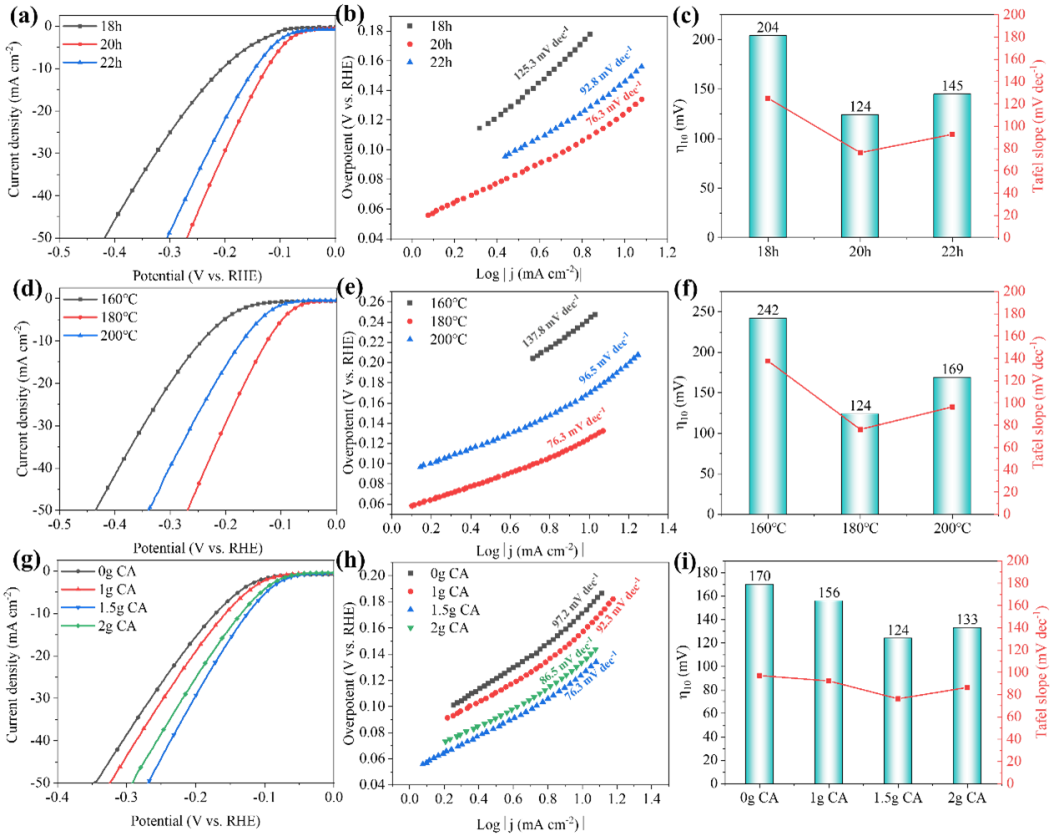

Figure 8. (a, d, g) The LSV curves and (b, e, h) the Tafel slopes and (c, f, i) performance comparison of α-MoC$_{1-x}$ prepared under different hydrothermal conditions.

During in-situ carburization of materials, carbon sources such as dicyandiamide and melamine, which decompose thermally to release gases and can form a carbon layer encapsulating the material, thereby preserving its structural stability. However, studies have shown that for core-shell structures, an excessively thick shell layer may hinder electron penetration to the catalyst, consequently impeding the catalytic process [38]. Figure 9a clearly demonstrates that in the initial stage, the carbon layer on the material surface gradually forms as the amount of dicyandiamide (DCD) increases. When the mass ratio of precursor to DCD reaches 1:2, the thickness of the carbon layer becomes optimal.

 doi:10.20944/preprints202601.0934.v1

Further increasing the DCD content leads to excessive carbon layer thickness, which adversely affects the material's hydrogen evolution performance, causing a decline in catalytic activity with increasing DCD amount. As the carbonization temperature rises, the material's performance progressively improves, reaching its peak catalytic activity at 800 °C. The Tafel slope plots (Figure 9(b, e)) of materials prepared under different DCD amounts and carbonization temperatures reveal that the sample with a 1:2 ratio and carbonized at 800 °C exhibits the lowest Tafel slope (76.3 mV dec^{-1}), which is consistent with previous characterization results. Consequently, these optimal preparation conditions were selected for vanadium doping, yielding polarization curves, the Tafel slopes, and performance comparison curves for different vanadium doping levels (Figure 9(g-I)).

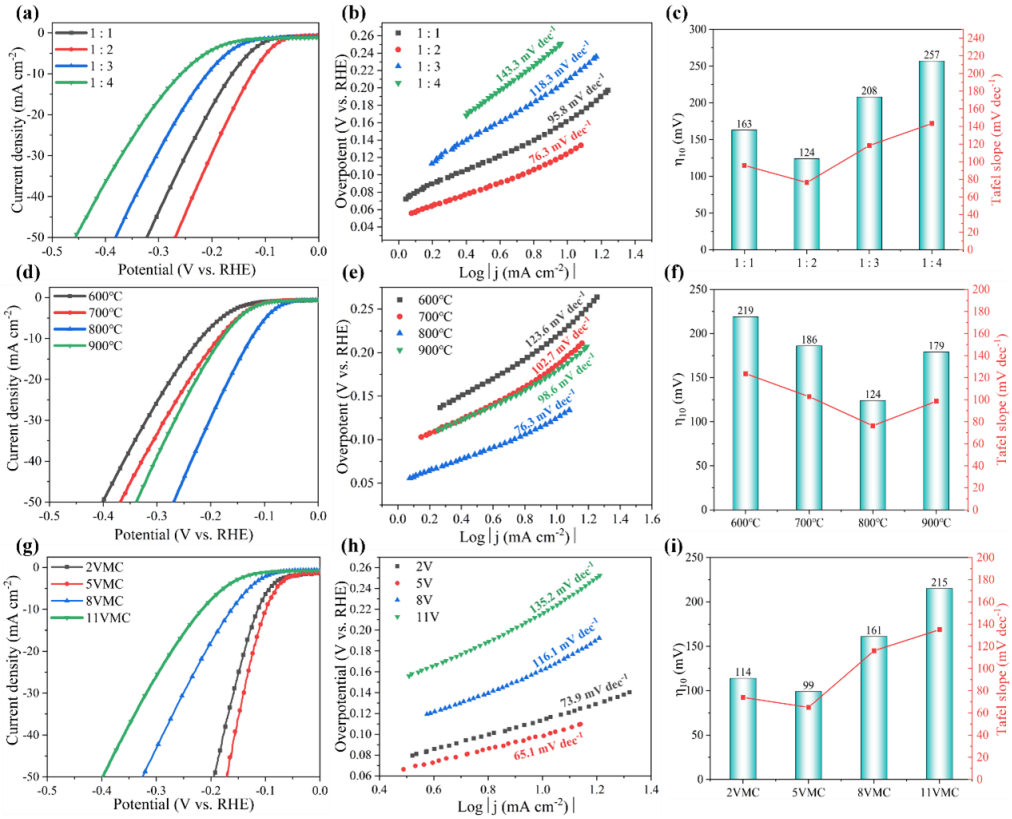

Figure 9. (a, d) The LSV curves and (b, e) the Tafel slopes and (c, f) comparative properties of α-MoC_{1-x} prepared under different carbonation conditions. (Hydrothermal treatment: 1.5 g citric acid, 800 °C, 20 h). Comparison of (g) the LSV curves and (h) the Tafel slopes and (i) η_{10} of V-Mo_xC prepared with different vanadium doping levels.

From the polarization curves in Figure 9g, it can be observed that the material with a Mo/V ratio of 100:5 achieves the lowest η_{10} (99 mV). The biphasic structure formed between α-MoC_{1-x} and β-Mo_2C introduces new active sites and modulates the surface properties of the catalyst, thereby enhancing catalytic activity. The η_{10} of the 2VMC sample (114 mV) also indicates that vanadium doping improves the hydrogen evolution performance compared to pure α-MoC_{1-x} (η_{10}: 124 mV). This suggests that vanadium not only regulates the biphasic structure but also intrinsically enhances the catalytic properties of molybdenum carbide. The Tafel slope analysis of vanadium-doped molybdenum carbides with different doping levels (Figure 9h) further confirms that 5VMC exhibits the lowest Tafel slope (65.1 mV dec^{-1}), surpassing that of the undoped sample. With increasing vanadium content, the HER performance of the material progressively declines. This degradation is likely attributable to an increase in the β-Mo_2C phase induced by the vanadium doping. Although β-Mo_2C is catalytically active, its high hydrogen adsorption energy impedes the efficient desorption of generated hydrogen gas. Consequently, hydrogen bubbles accumulate on the active sites, thereby slowing the overall reaction kinetics. This is reflected in the increasing overpotential observed with higher vanadium content. Furthermore, the performance trend indicates that the HER process

 doi:10.20944/preprints202601.0934.v1

follows the Volmer-Heyrovsky mechanism, with the electrochemical adsorption of water molecules (the Volmer step) being the rate-limiting process [39].

Electrochemical impedance spectroscopy (EIS) was employed to investigate the charge transfer mechanism, and the obtained Nyquist plots are shown in Figure 10. The smallest semicircle radius in the Nyquist plot was observed for the precursor prepared with 1.5 g of citric acid under hydrothermal conditions at 180 °C for 20 h, which was subsequently converted into α-MoC_{1-x}. This indicates the smallest charge transfer resistance (R_{ct}) and the fastest charge transfer rate, thereby facilitating the rapid progression of the HER. In the electrochemical impedance tests of catalysts synthesized with different dicyandiamide amounts and different carbonization temperatures, as shown in Figure 10(d, e), it can be observed that when the mass ratio of precursor to dicyandiamide is 1:2 and the carbonization temperature is 800 °C, the semicircle radius in the Nyquist plot is the smallest. This corresponds to the minimum R_{ct} and a high electron transfer rate, further confirming the optimal preparation conditions discussed earlier. The Figure 10f shows the EIS results of V-Mo_xC samples with different vanadium doping levels. The 5VMC sample exhibits the most favorable charge transfer kinetics, followed by the 2VMC, 8VMC, and 11VMC samples, which is consistent with their respective catalytic activities.

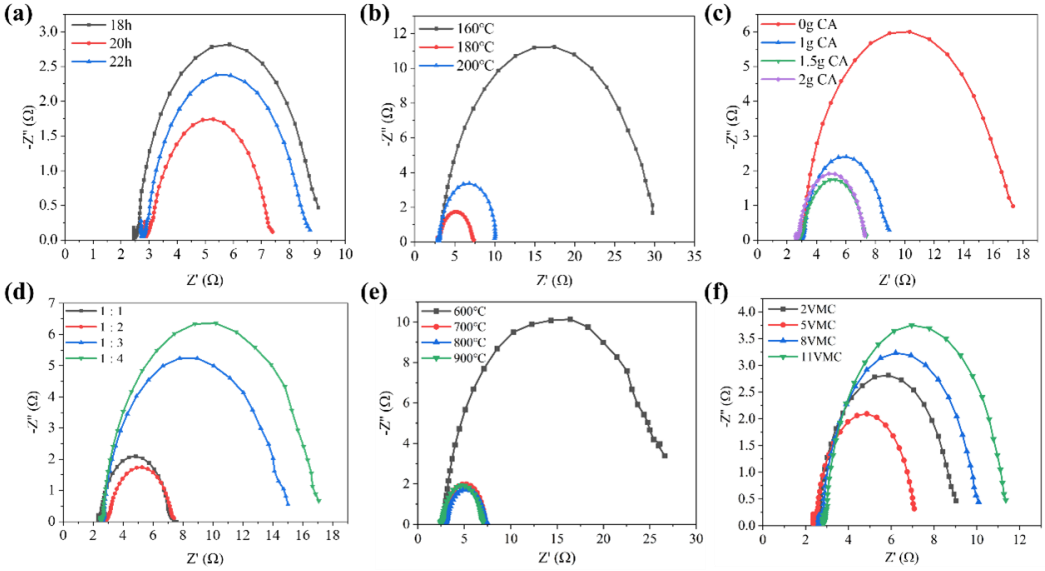

Figure 10. (a-e) Electrochemical impedance plots of α-MoC_{1-x} prepared under different hydrothermal and carbonation conditions. (f) Electrochemical impedance plots of V-Mo_xC prepared with different vanadium doping levels.

Figure 11(a-c) presents the double-layer capacitance (C_{dl}) measurements under three distinct hydrothermal conditions. It can be observed that the precursor obtained by adding 1.5 g of citric acid and undergoing hydrothermal treatment at 180 °C for 20 h exhibits the highest C_{dl}. Under subsequent carbonization conditions (Figure 11(d, e)), the material achieved its maximum electrochemical active surface area when the precursor-to-dicyandiamide mass ratio was 1:2 and the carbonization temperature was 800 °C, as reflected by the highest C_{dl} value of 14.9 mF cm^{-2}. This result further validates the optimal preparation conditions identified earlier. Subsequently, vanadium doping was performed under these optimized conditions, and the corresponding C_{dl} results are shown in Figure 11f. Among the four tested materials, the 5VMC sample exhibited the highest C_{dl} (16.7 mF cm^{-2}), confirming its ability to expose the largest effective active surface area during the catalytic process. This performance is superior to that of the undoped sample.

 doi:10.20944/preprints202601.0934.v1

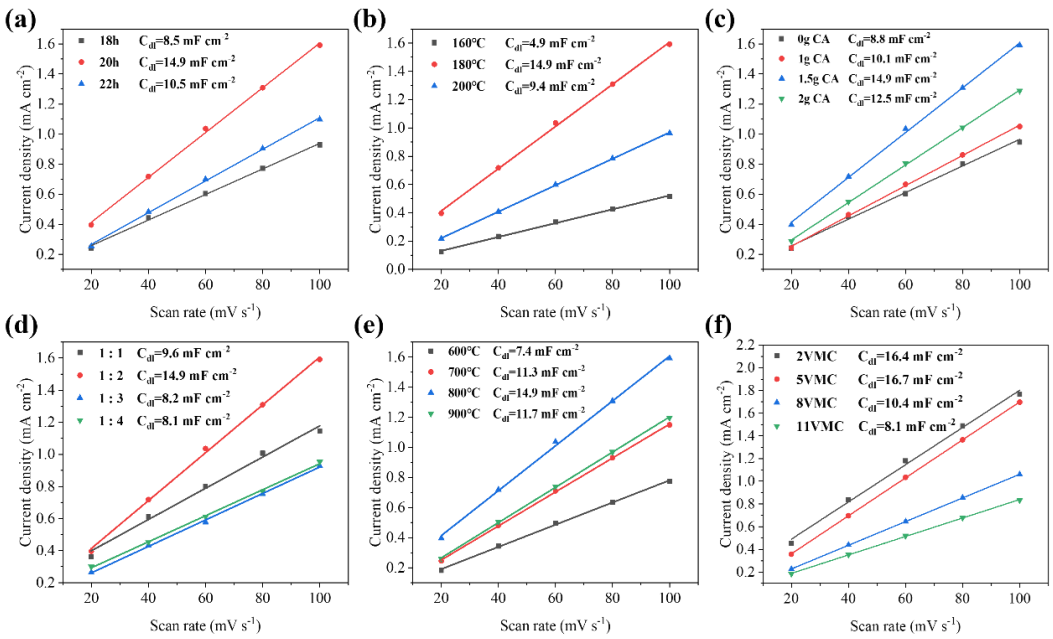

Figure 11. (a-e) Bilayer capacitance plots of α-MoC$_{1-x}$ prepared under different hydrothermal and carbonation conditions. (f) Bilayer capacitance plots of V-Mo$_x$C prepared with different vanadium doping levels.

Stability tests further demonstrate the durability of 5VMC. During the 100 h chronopotentiometric test at a constant current density of 10 mA cm^{-2}, as depicted in Figure 12a, the potential exhibits minimal fluctuation, while the Figure 12b reveals only a slight negative shift in the LSV curves after 1000 CV cycles. These results confirm the excellent long-term electrochemical stability of 5VMC.

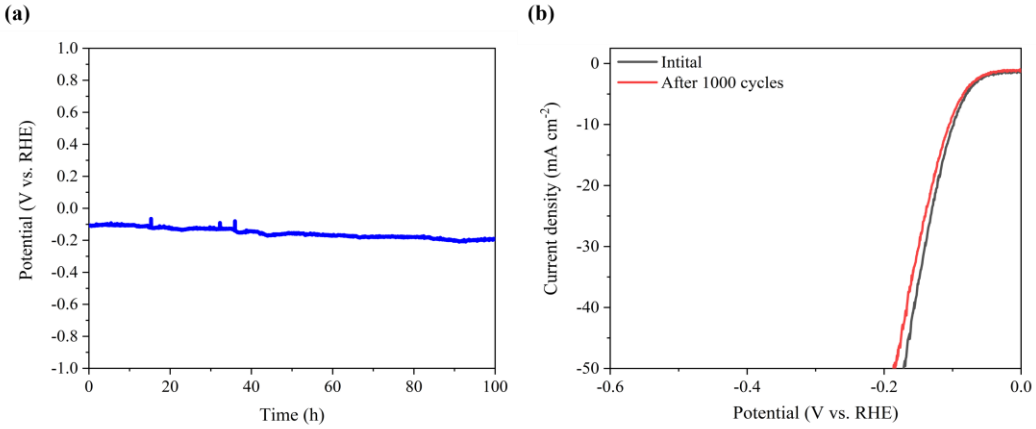

Figure 12. (a) Chrono-potential curves of 5VMC samples at 10 mA cm^{-2} and (b) the LSV curves before and after 1000 turns of CV cycling.

Table 1. Comparison of the performance of the present work with other HER electrocatalysts reported in the literature in 1 M KOH.

Catalysts	η_{10}/mV	Tafel slope/mV dec^{-1}	Ref.
V-Mo$_x$C	99	65.1	This work
MoC-Mo$_2$C-31.4 HNWs	120	42	[40]
Zn-MoC/Mo$_2$C-0.2	139	49.8	[41]

 doi:10.20944/preprints202601.0934.v1

MoC-Mo_2C	126	50	[42]
MoC-Mo_2C/PNCDs	121	60	[43]
MoC/Mo_2C (II)	112	69	[44]
Ni-Mo_xC/NC-100	162	104.8	[45]
Fe-MoC/β-Mo_2C@NC	143	73	[46]
Ni_{15}-Mo_2C/N	105	44.9	[47]

3. Materials and Methods

3.1. Materials and Chemicals

Ammonium molybdate tetrahydrate ($(NH_4)_6Mo_7O_{24}·4H_2O$), anhydrous citric acid ($C_6H_8O_7$), dicyandiamide ($C_2H_2N_4$), hydrofluoric acid (HF), ammonium metavanadate (NH_4VO_3) and anhydrous ethanol (CH_3CH_2OH) were bought from Shanghai Aladdin Biochemical Technology Co., Ltd. Silica (SiO_2 G.R.grade) was purchased from Sigma Aldrich Trading Co., Ltd. Nitric acid was bought from Xilong Fine Chemical Co., Ltd. Argon was provided by Henan Yuanzheng Technology Development Co., Ltd.

3.2. Synthesis of molybdenum carbide (α-MoC_{1-x}) Samples and Vanadium Doped MoxC (V-Mo_xC) Samples

A total of 0.5 g of SiO_2 was ultrasonically dispersed in 50 mL of deionized water. Subsequently, 5 mL of concentrated HNO_3 and 1.5 g of anhydrous citric acid were added under continuous stirring to ensure complete dissolution. After the solution became clear, 0.3 g of $(NH_4)_6Mo_7O_{24}·4H_2O$ was introduced, then the mixture was stirred thoroughly to achieve homogeneous dispersion of the precursors. The solution was transferred to a 100 mL Teflon-lined autoclave and heated at 180 °C for 20 h. After washing and vacuum drying at 60 °C, the molybdenum oxide precursor loaded with SiO_2 was obtained. Each precursor (200 mg) was placed downstream in a quartz boat, with 400 mg $C_2H_2N_4$ upstream. Under Ar gas, the furnace was heated to 500 °C (2 °C/min, insulated for 1 h), then to 800 °C (5 °C/min, insulated for 2 h). After cooling, the SiO_2 template was removed with 10% HF/ethanol, and the products were washed and dried to yield α-MoC_{1-x}. The preparation scheme of α-MoC_{1-x} was illustrated in Figure 1a.

After adding $(NH_4)_6Mo_7O_{24}·4H_2O$ in the aforementioned steps, measured quantities of ammonium metavanadate (with Mo/V molar ratios of 100:2, 100:5, 100:8, and 100:11) were introduced into the solution under continuous stirring. By repeating the subsequent procedures described above, V-Mo_xC samples were obtained. These samples were designated as 2VMC, 5VMC, 8VMC, and 11VMC according to their respective vanadium doping concentrations.

3.3. Materials characterization

The Bruker AXS D8 Advance X-ray diffractometer with Cu Kα radiation was served to measure X-ray diffraction (XRD) results. The scanning range was 10-80°, and the step size was 0.02°. The Raman spectra (Horiba LabRAM HR Evolution) of the composites were investigated with a laser diode at an excitation wavelength of 532 nm. Meanwhile, using the Micromeritics ASAP 2020 adsorbent to obtain the specific surface area of the material. In addition, the morphology and microstructures of the catalyst was determined by scanning electron microscope (JMS-75000F), transmission electron microscope (Talos™ F200). By analyzing X-ray photoelectron spectroscopy (Escalab-250Xi), quantitative analysis of elements and information on electronic energy level structure can be gained.

3.4. Electrochemical measurements

 doi:10.20944/preprints202601.0934.v1

All electrochemical measurements were conducted in 1.0 M KOH using a typical three-electrode setup with a DH-7000 workstation (Donghua Analytical Instrument Co., Ltd., Jiangsu). The prepared catalyst, a platinum plate, and an Hg/HgO electrode served as the working, counter, and reference electrodes, respectively. 2.5 mg of the catalyst was added to a mixture of 245 μL deionized water, 245 μL anhydrous ethanol, and 10 μL of a 5 wt% Nafion dispersion. The mixture was sonicated for 1 h to form a homogeneous ink. Then, 150 μL of the ink was drop-cast onto an alcohol-washed and dried carbon paper (0.5×2 cm), covering an area of 0.5×1 cm to achieve a catalyst loading of approximately 0.75 mg cm^{-2}. After thorough drying, the prepared electrode was used as the working electrode. All potentials were converted to the reversible hydrogen electrode (RHE) scale using: E (vs. RHE) = E (vs. Hg/HgO) + 0.098 + 0.0592 × pH. Linear sweep voltammetry (LSV) was performed from −0.8 to −1.3 V at 5 mV s^{-1} to obtain polarization curves. Tafel slopes were derived from the LSV data using the Tafel equation ($\eta = b \cdot \log|j| + a$). Cyclic voltammetry (CV) was conducted within a potential window of −0.45 to −0.35 V. The material was first scanned continuously until a stable response was obtained. Subsequently, CV scans were performed at scan rates ranging from 20 to 100 mV s^{-1} with an increment of 20 mV s^{-1}, and with 10 cycles recorded at each rate. The data from the last cycle at each scan rate were used for analysis. The Electrochemical impedance spectroscopy (EIS) measurements were performed over a frequency range of 10^{-2} to 10^{5} Hz with an amplitude of 5 mV.

4. Conclusions

In summary, α phase and α/β dual-phase composite structured molybdenum carbide electrocatalysts were successfully prepared, and vanadium doping improved their catalytic performance. Firstly, the optimal preparation method for the α phase was obtained through continuous optimization of the preparation process. The α-MoC_{1-x} obtained at a hydrothermal temperature of 180 °C, hydrothermal time of 20 h, citric acid addition of 1.5 g, carbonization conditions of 800 °C, and precursor/dicyandiamide mass ratio of 1:2 exhibited the best electrocatalytic hydrogen evolution performance. Vanadium doped biphasic molybdenum carbide catalyst was prepared by introducing vanadium during the above preparation process. The addition of vanadium causes the transformation of molybdenum carbide from the α phase to the β phase. After the addition of vanadium, the catalyst structure becomes fragmented, the thickness decreases, and the specific surface area of the material increases. The V-Mo_xC catalyst with a Mo/V molar ratio of 100:5 exhibits the best charge transfer kinetics and surface properties, with a β/α ratio of 0.827. Due to the advantages of biphasic catalysts, V-Mo_xC catalysts exhibit superior hydrogen evolution performance, with an η_{10} of 99 mV, a Tafel slope of 65.1 mV dec^{-1}, and excellent stability.

Author Contributions: S.L.: Writing-review & editing, Project administration, Funding acquisition. Y.L.: Conceptualization, Methodology, Data curation, Writing-original draft. R.J.: Validation, Formal Analysis. J.W.: Visualization, Formal Analysis. P.Z.: Investigation, Visualization. J.W.: Investigation, Resources. X.Y.: Supervision, Writing-Review & Editing. J.Z.: Project Administration, Writing-Review & Editing. All authors have read and agreed to the published version of the manuscript.

Funding: This work was supported by the Outstanding Young Talents Innovation Team Project of Zhengzhou University.

Data Availability Statement: The data presented in this study are available on request from the corresponding author.

Conflicts of Interest: The authors declare no conflicts of interest.

References

1. Jin, J.;Wang, X.;Hu, Y.;Zhang, Z.;Liu, H.;Yin, J. and Xi, P. Precisely Control Relationship between Sulfur Vacancy and H Absorption for Boosting Hydrogen Evolution Reaction, Nano-Micro Letters.2024, 16, 63.10.1007/s40820-023-01291-3

 doi:10.20944/preprints202601.0934.v1

2. Iqbal, M. Z.;Zahid, R.;Khan, M. W.;Shaheen, M.;Aziz, U. and Aftab, S. Exploration of catalytically active materials for efficient electrochemical hydrogen and oxygen evolution reactions, International Journal of Hydrogen Energy.2023, 48, 8045-8070. https://doi.org/10.1016/j.ijhydene.2022.11.121
3. Bender, J. T.;Petersen, A. S.;Østergaard, F. C.;Wood, M. A.;Heffernan, S. M. J.;Milliron, D. J.;Rossmeisl, J. and Resasco, J. Understanding Cation Effects on the Hydrogen Evolution Reaction, ACS Energy Letters.2023, 8, 657-665.10.1021/acsenergylett.2c02500
4. Huang, C.;Ouyang, T.;Zou, Y.;Li, N. and Liu, Z. Q. Ultrathin $NiCo_2P_x$ nanosheets strongly coupled with CNTs as efficient and robust electrocatalysts for overall water splitting, Journal of Materials Chemistry A.2018, 10.1039.C1037TA11364A
5. Gong, Q.;Cheng, L.;Liu, C.;Zhang, M.;Feng, Q.;Ye, H.;Zeng, M.;Xie, L.;Liu, Z. and Li, Y. Ultrathin $MoS_{2(1-x)}Se2_x$ Alloy Nanoflakes For Electrocatalytic Hydrogen Evolution Reaction, ACS Catalysis.2015, 5, 2213-2219.10.1021/cs501970w
6. Sun, J.;Chen, Y.;Ren, Z.;Fu, H.;Xiao, Y.;Wang, J. and Tian, G. Self-Supported NiS Nanoparticle-Coupled Ni_2P Nanoflake Array Architecture: An Advanced Catalyst for Electrochemical Hydrogen Evolution, ChemElectroChem.2017, 4, 1341-1348. https://doi.org/10.1002/celc.201700094
7. Guo, Y.;Zhou, X.;Tang, J.;Tanaka, S.;Kaneti, Y. V.;Na, J.;Jiang, B.;Yamauchi, Y.;Bando, Y. and Sugahara, Y. Multiscale structural optimization: Highly efficient hollow iron-doped metal sulfide heterostructures as bifunctional electrocatalysts for water splitting, Nano Energy.2020, 75, 104913. https://doi.org/10.1016/j.nanoen.2020.104913
8. Bui, H. T.;Lam, N. D.;Linh, D. C.;Mai, N. T.;Chang, H.;Han, S.-H.;Oanh, V. T. K.;Pham, A. T.;Patil, S. A.;Tung, N. T. and Shrestha, N. K. Escalating Catalytic Activity for Hydrogen Evolution Reaction on $MoSe_2$@Graphene Functionalization, Nanomaterials.2023, 13, 2139
9. Lin, L.;Yao, S.;Gao, R.;Liang, X.;Yu, Q.;Deng, Y.;Liu, J.;Peng, M.;Jiang, Z.;Li, S.;Li, Y.-W.;Wen, X.-D.;Zhou, W. and Ma, D. A highly CO-tolerant atomically dispersed Pt catalyst for chemoselective hydrogenation, Nature Nanotechnology.2019, 14, 354-361.10.1038/s41565-019-0366-5
10. Chen, M.;Ma, Y.;Zhou, Y.;Liu, C.;Qin, Y.;Fang, Y.;Guan, G.;Li, X.;Zhang, Z. and Wang, T. Influence of Transition Metal on the Hydrogen Evolution Reaction over Nano-Molybdenum-Carbide Catalyst, Catalysts.2018, 8, 294
11. Ni, J.;Ruan, Z.;Xu, J.;Yan, J.;Ma, J.;Ma, H.;Qi, J.;Zhu, S. and Lu, L. Regulating surface wettability and electronic state of molybdenum carbide for improved hydrogen evolution reaction, International Journal of Hydrogen Energy.2023, 48, 17478-17488. https://doi.org/10.1016/j.ijhydene.2023.01.245
12. Xia, K.;Guo, J.;Xuan, C.;Huang, T.;Deng, Z.;Chen, L. and Wang, D. Ultrafine molybdenum carbide nanoparticles supported on nitrogen doped carbon nanosheets for hydrogen evolution reaction, Chinese Chemical Letters.2019, 30, 192-196. https://doi.org/10.1016/j.cclet.2018.05.009
13. Kitchin, J. R.;Nørskov, J. K.;Barteau, M. A. and Chen, J. G. Trends in the chemical properties of early transition metal carbide surfaces: A density functional study, Catalysis Today.2005, 105, 66-73. https://doi.org/10.1016/j.cattod.2005.04.008
14. Li, S.;Su, S.;Tian, Y.;Li, Y.;Yu, X.;Sun, P. and Zheng, J. Y. Template-assisted preparation of imbricate N–Mo_xC nanotubes for the effective electrocatalytic hydrogen evolution reaction, CrystEngComm. 2023, 25, 1648-1656.10.1039/D2CE01454H
15. Yu, X.;Shi, W.;Wei, J.;Liu, T.;Li, Y.;He, M.;Wei, Z.;Ping, D.;Sun, P.;Zheng, J. Y. and Li, S. Green fabrication of ultrafine N-Mo_xC/CoP hybrids for boosting electrocatalytic water reduction, Nanotechnology.2024, 35, 065704.10.1088/1361-6528/ad0985
16. Politi, J. R. d. S.;Viñes, F.;Rodriguez, J. A. and Illas, F. Atomic and electronic structure of molybdenum carbide phases: bulk and low Miller-index surfaces, Physical Chemistry Chemical Physics.2013, 15, 12617-12625.10.1039/C3CP51389K
17. Gao, Q.;Zhang, W.;Shi, Z.;Yang, L. and Tang, Y. Structural Design and Electronic Modulation of Transition-Metal-Carbide Electrocatalysts toward Efficient Hydrogen Evolution, Advanced Materials.2019, 31, 1802880. https://doi.org/10.1002/adma.201802880

 doi:10.20944/preprints202601.0934.v1

18. Hunt, S. T.;Milina, M.;Alba-Rubio, A. C.;Hendon, C. H.;Dumesic, J. A. and Román-Leshkov, Y. Self-assembly of noble metal monolayers on transition metal carbide nanoparticle catalysts, Science.2016, 352, 974-978.doi:10.1126/science.aad8471
19. Vrubel, H. and Hu, X. Molybdenum Boride and Carbide Catalyze Hydrogen Evolution in both Acidic and Basic Solutions, Angewandte Chemie International Edition.2012, 51, 12703-12706. https://doi.org/10.1002/anie.201207111
20. Wan, C.;Regmi, Y. N. and Leonard, B. M. Multiple Phases of Molybdenum Carbide as Electrocatalysts for the Hydrogen Evolution Reaction, Angewandte Chemie.2014, 126, 6525-6528. https://doi.org/10.1002/anie.201402998
21. Gong, Q.;Wang, Y.;Hu, Q.;Zhou, J.;Feng, R.;Duchesne, P. N.;Zhang, P.;Chen, F.;Han, N.;Li, Y.;Jin, C.;Li, Y. and Lee, S.-T. Ultrasmall and phase-pure W_2C nanoparticles for efficient electrocatalytic and photoelectrochemical hydrogen evolution, Nature Communications. 2016, 7,13216. https://doi.org/10.1038/ncomms13216
22. Yu, F.;Gao, Y.;Lang, Z.;Ma, Y.;Yin, L.;Du, J.;Tan, H.;Wang, Y. and Li, Y. Electrocatalytic performance of ultrasmall Mo_2C affected by different transition metal dopants in hydrogen evolution reaction, Nanoscale. 2018, 10, 6080-6087.10.1039/C8NR00908B
23. Wu, T.;Zhang, J.;Chen, Y.;Jia, Y.;An, J.;Ge, J. and Wang, M. Simple and Controllable Preparation of Molybdenum Carbides by One-Step Co-Electrolysis of Na_2MoO_4 and CO_2, Journal of The Electrochemical Society. 2023, 170, 053503.10.1149/1945-7111/acd0d9
24. Chen, Z.;Guo, T.;Wu, Z. and Wang, D. Boron triggers the phase transformation of Mo_xC (α-MoC_{1-x}/β-Mo_2C) for enhanced hydrogen production, Nanotechnology.2020, 31, 105707.10.1088/1361-6528/ab5a25
25. Baek, D. S.;Jung, G. Y.;Seo, B.;Kim, J. C.;Lee, H.-W.;Shin, T. J.;Jeong, H. Y.;Kwak, S. K. and Joo, S. H. Ordered Mesoporous Metastable α-MoC_{1-x} with Enhanced Water Dissociation Capability for Boosting Alkaline Hydrogen Evolution Activity, Advanced Functional Materials.2019, 29, 1901217. https://doi.org/10.1002/adfm.201901217
26. Li, Y.;Jia, B.;Fan, Y.;Zhu, K.;Li, G. and Su, C.-Y. Bimetallic Zeolitic Imidazolite Framework Derived Carbon Nanotubes Embedded with Co Nanoparticles for Efficient Bifunctional Oxygen Electrocatalyst, Advanced Energy Materials.2018, 8, 1702048. https://doi.org/10.1002/aenm.201702048
27. Schweitzer, N. M.;Schaidle, J. A.;Ezekoye, O. K.;Pan, X.;Linic, S. and Thompson, L. T. High Activity Carbide Supported Catalysts for Water Gas Shift, Journal of the American Chemical Society.2011, 133, 2378-2381. https://doi.org/10.1021/ja110705a
28. Zhang, Y.;Liu, X.;Li, W.;Liu, W.;Yin, H. and Wang, D. Advanced and Durable Self-Standing MoC-Mo_2C Electrode for Alkaline Hydrogen Evolution in Chlor-alkali Electrolysis, ACS Sustainable Chemistry & Engineering.2023, 11, 9470-9477.10.1021/acssuschemeng.3c01721
29. Huang, Y.;Hu, J.;Xu, H.;Bian, W.;Ge, J.;Zang, D.;Cheng, D.;Lv, Y.;Zhang, C.;Gu, J. and Wei, Y. Fine Tuning Electronic Structure of Catalysts through Atomic Engineering for Enhanced Hydrogen Evolution, Advanced Energy Materials.2018, 8, 1800789. https://doi.org/10.1002/aenm.201800789
30. Zang, D.;Gao, X. J.;Li, L.;Wei, Y. and Wang, H. Confined interface engineering of self-supported Cu@N-doped graphene for electrocatalytic CO_2 reduction with enhanced selectivity towards ethanol, Nano Research.2022, 15, 8872-8879.10.1007/s12274-022-4698-3
31. Xu, H.;Jia, H.;Fei, B.;Ha, Y.;Li, H.;Guo, Y.;Liu, M. and Wu, R. Charge Transfer Engineering via Multiple Heteroatom Doping in Dual Carbon-Coupled Cobalt Phosphides for Highly Efficient Overall Water Splitting, Applied Catalysis B: Environmental.2020, 268, 118404. https://doi.org/10.1016/j.apcatb.2019.118404
32. Zhao, T.;Jia, Z.;Zhang, Y. and Wu, G. Multiphase Molybdenum Carbide Doped Carbon Hollow Sphere Engineering: The Superiority of Unique Double-Shell Structure in Microwave Absorption, Small.2023, 19, 2206323. https://doi.org/10.1002/smll.202206323
33. Chen, Y.-Y.;Zhang, Y.;Jiang, W.-J.;Zhang, X.;Dai, Z.;Wan, L.-J. and Hu, J.-S. Pomegranate-like N,P-Doped Mo_2C@C Nanospheres as Highly Active Electrocatalysts for Alkaline Hydrogen Evolution, ACS Nano.2016, 10, 8851-8860.10.1021/acsnano.6b04725

34. Lu, X. F.;Yu, L.;Zhang, J. and Lou, X. W. D. Ultrafine Dual-Phased Carbide Nanocrystals Confined in Porous Nitrogen-Doped Carbon Dodecahedrons for Efficient Hydrogen Evolution Reaction, Adv Mater.2019, 31, e1900699.10.1002/adma.201900699
35. Cui, W.;Cheng, N.;Liu, Q.;Ge, C.;Asiri, A. M. and Sun, X. Mo_2C Nanoparticles Decorated Graphitic Carbon Sheets: Biopolymer-Derived Solid-State Synthesis and Application as an Efficient Electrocatalyst for Hydrogen Generation, ACS Catalysis.2014, 4, 2658-2661.10.1021/cs5005294
36. Wang, D.;Zhang, X.;Bao, S.;Zhang, Z.;Fei, H. and Wu, Z. Phase engineering of a multiphasic 1T/2H MoS_2 catalyst for highly efficient hydrogen evolution, Journal of Materials Chemistry A.2017, 5, 2681-2688.10.1039/C6TA09409K
37. Huang, J.;Wang, J.;Xie, R.;Tian, Z.;Chai, G.;Zhang, Y.;Lai, F.;He, G.;Liu, C.;Liu, T.;Shearing, P. R. and Brett, D. J. L. A universal pH range and a highly efficient Mo_2C-based electrocatalyst for the hydrogen evolution reaction, Journal of Materials Chemistry A.2020, 8, 19879-19886.10.1039/D0TA07091B
38. Jiang, H.;Yan, L.;Zhang, S.;Zhao, Y.;Yang, X.;Wang, Y.;Shen, J.;Zhao, X. and Wang, L. Electrochemical Surface Restructuring of Phosphorus-Doped Carbon@MoP Electrocatalysts for Hydrogen Evolution, Nano-Micro Letters.2021, 13, 215.10.1007/s40820-021-00737-w
39. Liu, M.-J.;Yang, F.-H.;Mei, J.-C.;Guo, X.;Wang, H.-Y.;He, M.-Y.;Yao, Y.-A.;Zhang, H.-F. and Liu, C.-B. MOF Template-Derived Carbon Shell-Embedded CoP Hierarchical Nanosheet as Bifunctional Catalyst for Overall Water Splitting, Nanomaterials.2023, 13, 2421
40. Sun, J.;Zhang, X.;Jin, M.;Xiong, Q.;Wang, G.;Zhang, H. and Zhao, H. Robust enhanced hydrogen production at acidic conditions over molybdenum oxides-stabilized ultrafine palladium electrocatalysts, Nano Research.2021, 14, 268-274.10.1007/s12274-020-3083-3
41. Li, X.;Jiang, Y.;Jia, L. and Wang, C. MoO_2 nanoparticles on reduced graphene oxide/polyimide-carbon nanotube film as efficient hydrogen evolution electrocatalyst, Journal of Power Sources.2016, 304, 146-154. https://doi.org/10.1016/j.jpowsour.2015.11.013
42. Wu, L.;Wang, X.;Sun, Y.;Liu, Y. and Li, J. Flawed MoO_2 belts transformed from MoO_3 on a graphene template for the hydrogen evolution reaction, Nanoscale.2015, 7, 7040-7044.10.1039/C4NR06624C
43. Jin, Y.;Wang, H.;Li, J.;Yue, X.;Han, Y.;Shen, P. K. and Cui, Y. Porous MoO_2 Nanosheets as Non-noble Bifunctional Electrocatalysts for Overall Water Splitting, Advanced Materials.2016, 28, 3785-3790. https://doi.org/10.1002/adma.201506314
44. Sun, C.;Wang, P.;Wang, H.;Xu, C.;Zhu, J.;Liang, Y.;Su, Y.;Jiang, Y.;Wu, W.;Fu, E. and Zou, G. Defect engineering of molybdenum disulfide through ion irradiation to boost hydrogen evolution reaction performance, Nano Research. 2019, 12, 1613-1618.10.1007/s12274-019-2400-1
45. Saleem, S.;Salman, M.;Ali, S.;Ling, Y. and Khan, M. Electrocatalytic hydrogen evolution reaction on sulfur-deficient MoS_2 nanostructures, International Journal of Hydrogen Energy.2022, 47, 7713-7723. https://doi.org/10.1016/j.ijhydene.2021.12.081
46. Ghosh, D.;Ghosal Chowdhury, M.;Biswas, R.;Haldar, K. K. and Patra, A. Europium Molybdate/Molybdenum Disulfide Nanostructures with Efficient Electrocatalytic Activity for the Hydrogen Evolution Reaction, ACS Applied Nano Materials.2023, 6, 7218-7228.10.1021/acsanm.3c00297
47. Huang, Y.;Wang, C.;Song, H.;Bao, Y. and Lei, X. Carbon-coated molybdenum carbide nanosheets derived from molybdenum disulfide for hydrogen evolution reaction, International Journal of Hydrogen Energy.2018, 43, 12610-12617. https://doi.org/10.1016/j.ijhydene.2018.03.233